

Modeling the evaporation of sessile multi-component droplets



C. Diddens^{a,*}, J.G.M. Kuerten^{a,b}, C.W.M. van der Geld^c, H.M.A. Wijshoff^{a,d}

^a Department of Mechanical Engineering, Eindhoven University of Technology, P.O. Box 513, 5600 MB Eindhoven, The Netherlands

^b Faculty EEMCS, University of Twente, P.O. Box 217, 7500 AE Enschede, The Netherlands

^c Department of Chemical Engineering and Chemistry, Eindhoven University of Technology, P.O. Box 513, 5600 MB Eindhoven, The Netherlands

^d Océ-Technologies B.V., P.O. Box 101, 5900 MA Venlo, The Netherlands

GRAPHICAL ABSTRACT

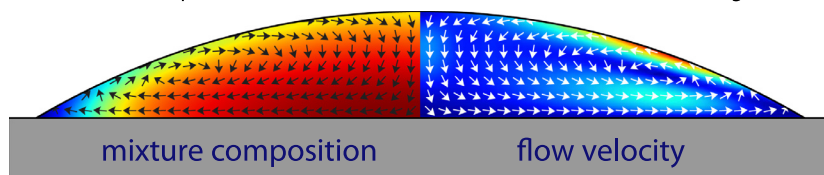
Evaporation of Multi-Component Droplets

preferential evaporation

non-uniform composition

surface tension gradient

solutal Marangoni flow



ARTICLE INFO

Article history:

Received 18 August 2016

Revised 13 October 2016

Accepted 14 October 2016

Available online 20 October 2016

Keywords:

Droplets

Lubrication approximation

Multi-component flow

Evaporation

Marangoni flow

ABSTRACT

We extended a mathematical model for the drying of sessile droplets, based on the lubrication approximation, to binary mixture droplets. This extension is relevant for e.g. inkjet printing applications, where ink consisting of several components are used. The extension involves the generalization of an established vapor diffusion-limited evaporation model to multi-component mixtures. The different volatilities of the liquid components generate a composition gradient at the liquid-air interface. The model takes the composition-dependence of the mass density, viscosity, surface tension, mutual diffusion coefficient and thermodynamic activities into account. This leads to a variety of effects ranging from solutal Marangoni flow over deviations from the typical spherical cap shape to an entrapped residual amount of the more volatile component at later stages of the drying. These aspects are discussed in detail on the basis of the numerical results for water-glycerol and water-ethanol droplets. The results show good agreement with experimental findings. Finally, the accuracy of the lubrication approximation is assessed by comparison with a finite element method.

© 2016 Elsevier Inc. All rights reserved.

1. Introduction

Because of the widespread range of applications, ranging from inkjet printing [1] and spray cooling [2] to the deposition of protein molecules on microarray slides [3] and more, the evaporation of sessile droplets in ambient gas has aroused significant interest in

* Corresponding author.

E-mail address: C.Diddens@tue.nl (C. Diddens).

the latest decades. Although this represents a ubiquitous and classical phenomenon, the underlying physics, comprising the evaporation rate, the flow in the droplet and the dynamics at the contact line, is rather complex and still subject of ongoing research.

A substantial contribution to the theoretical understanding of the drying of droplets was achieved by Deegan et al. [4,5] and Popov [6]. They found that the evaporation rate is essentially controlled by the diffusion of vapor from the droplet surface to the ambient, which results in a non-homogeneous evaporation rate

with a singularity at the contact line. Based on this model, a variety of numerical and analytical investigations were carried out [7–14].

While the temperature-driven Marangoni flow or the presence of solute particles and their deposition to the substrate have been taken into account in some of these studies, they were confined to droplets consisting of a pure fluid. In applications like inkjet printing, however, the ink is typically a mixture of a solvent and various co-solvents, as well as surfactants and possibly colloidal solute particles. Experimentally, it has been shown that the evaporation of a binary mixture droplet can exhibit interesting non-monotonic behavior of the contact angle [15–19], initial condensation of water from the surrounding air [20] and presumably an entrapped residual amount of the more volatile component [21,22]. Furthermore, Christy et al. [23] and Bennacer and Sefiane [24] revealed by particle image velocimetry that evaporating water-ethanol droplets undergo flow transitions: initially, in regime I, the preferential evaporation of ethanol triggers a solutal Marangoni flow that drives a complicated non-axisymmetric flow with multiple vortices in the droplet. After that, they observed a rapid transition with an intense velocity peak (regime II) followed by the usual capillary flow to the contact line as in the case of pure droplets (regime III). Recently, Zhong and Duan showed that the duration of the transition regime II can also last for rather long time, where they observed a nearly axisymmetric Marangoni flow [25].

Binary mixture droplets can also be combined with surfactants and surface-absorbed polymers to create homogeneous deposition patterns [26]. Beyond that, Cira et al. have recently shown that neighboring binary mixture droplets can interact through the vapor phase which allows the assembly of autonomous fluidic machines [27].

The present study attempts to reveal for the first time the underlying physical phenomena in a single axisymmetric binary mixture droplet by mathematical modeling and subsequent comparison with experiments. A mathematical model for the evaporation of sessile binary mixture droplets faces two challenges. On the one hand, the established diffusion-limited evaporation model has to be generalized to mixtures. As already mentioned by Guéna et al. [28] and as will be shown in this work, the local evaporation rate of each liquid will not only depend on the local liquid composition at the considered position of the interface, but on the entire concentration distribution along the liquid-air interface. On the other hand, the physical properties of the liquid in the droplet, i.e. mass density, viscosity, surface tension and mutual diffusion coefficient, depend on the local fluid composition. While these properties can be treated as constants for pure fluids (except for a temperature-dependent surface tension), the flow in the mixture droplet is governed by an interplay of preferential evaporation at the liquid-air interface, convection and diffusion of the non-uniform composition and the corresponding spatio-temporally varying physical properties of the fluid. Of course, all this combined makes an analytical solution practically impossible.

In this study we present the to our knowledge first model for the drying of a sessile binary mixture droplet which comprises all these necessary generalizations. Nevertheless, by considering axisymmetric droplets with small contact angles and taking advantage of an extended lubrication approximation, the underlying equations are relatively simple so that the computational effort is modest, even for full solutions in a considerable time domain. We will, however, also assess the accuracy of the lubrication approximation by a comparison with a finite-element model applied to the full Stokes flow.

The article is organized as follows: the multi-component lubrication theory and the generalized evaporation model are described in Section 2. Typical results for water-glycerol and water-ethanol droplets are discussed in Sections 3 and 4, respectively. In Section 5,

we carefully discuss the accuracy of the lubrication approach by comparing its results with results of finite element simulations.

2. Modeling

2.1. Droplet

The model is an extension of previous work by Siregar et al. [10]. The droplet is assumed to be axisymmetric and is described in cylindrical coordinates (r, z) with corresponding fluid velocity components (u, w) . The contact angle θ must be rather small because of the subsequent lubrication approximation. With this assumption, the liquid-air interface Γ can be written in Monge's form

$$\Gamma(t) = \{(r, z) | z = h(r, t)\}, \quad (1)$$

so that the evolution of the droplet shape is given by the height function $h(r, t)$, where the substrate has been set to $z = 0$ (see Fig. 1 for an illustration). For the moment, only the liquid region, i.e. $0 < z < h(r, t)$, is considered. The gas phase will become relevant for the evaporation model in Section 2.4.

2.2. Mixture

The liquid composition is denoted in terms of the mass fractions y_A and y_B of liquid A and B, respectively, where A and B are assumed to be miscible. If the mass averaged velocity \mathbf{v} is known, the mass fractions $y_v(r, z, t)$ (with $v = A, B$) evolve according to (see e.g. [29])

$$\rho(\partial_t y_v + \mathbf{v} \cdot \nabla y_v) = \nabla \cdot (\rho D_{AB} \nabla y_v) - \dot{m}_v \delta_\Gamma. \quad (2)$$

Here, ρ is the total mass density of the mixture and D_{AB} is the mutual diffusion coefficient which are both functions of y_v . δ_Γ is the interface delta function and \dot{m}_v is a sink term which arises due to the evaporative mass flux. A quantification of the latter will be given in Section 2.4.

The composition-dependence of the mass density ρ , the viscosity μ , the surface tension σ and the diffusion coefficient D_{AB} must be specified according to experimental data for the actual mixture. When the functional relationships between the composition and these quantities are given, the latter can be written as functions of space and time, i.e. $\rho(r, z, t)$, $\mu(r, z, t)$, $\sigma(r, t)$ and $D_{AB}(r, z, t)$.

2.3. Lubrication approximation

Since the mass density ρ depends on the local composition, the derivation of the model has to start with the full Navier-Stokes momentum equation with non-constant density and the conservation equations for both constituents, from which (2) and the usual

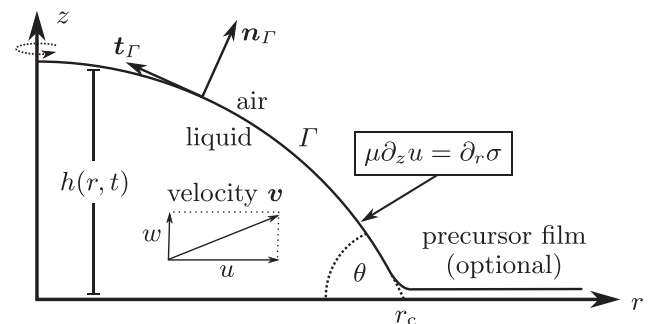


Fig. 1. Schematic sketch of the axisymmetric droplet. In case of an unpinned contact line, a precursor film is considered (cf. Section 5.4). A Marangoni shear stress is imposed at the liquid-air interface Γ .

continuity equation for ρ can be derived. For the moment, an energy equation is not considered, i.e. it is assumed that the latent heat of evaporation is conducted sufficiently rapidly so that the process can be considered as approximately isothermal. We briefly discuss thermal influences later on in Section 4.2.2.

When the droplet is rather flat, i.e. the contact angle θ is small, and in the limit of a low Reynolds number, the so called lubrication approximation can be applied (see e.g. [30,31]). For the case with non-uniform viscosity $\mu(r, z, t)$ and mass density $\rho(r, z, t)$, one obtains the following set of governing equations:

$$\frac{\partial p}{\partial r} = \frac{\partial}{\partial z} \left(\mu \frac{\partial u}{\partial z} \right), \quad (3)$$

$$\frac{\partial p}{\partial z} = 0, \quad (4)$$

$$\frac{\partial \rho}{\partial t} + \frac{1}{r} \frac{\partial}{\partial r} (r \rho u) + \frac{\partial}{\partial z} (\rho w) = 0. \quad (5)$$

Here, gravitational forces were neglected by the assumption that the considered droplet size is small compared to the capillary length. While the flow is treated in its steady limit, the $\frac{\partial \rho}{\partial t}$ term is important in the continuity equation to ensure mass conservation for a mixture with a composition-dependent mass density.

The pressure p in (3) and (4) is given by the Laplace pressure

$$p = p_L = -\sigma \frac{1}{r} \frac{\partial}{\partial r} \left(\frac{r \partial_r h}{\sqrt{1 + (\partial_r h)^2}} \right), \quad (6)$$

where the square root in the denominator has to be approximated by unity in the limit of the lubrication approximation.

At the liquid-air interface Γ , a surface tension gradient will cause a shear stress that drives a Marangoni flow. To the order of the lubrication approximation, this boundary condition reads

$$\mu \partial_z u = \partial_r \sigma. \quad (7)$$

Integrating Eq. (3) yields the radial velocity

$$u(r, z, t) = \int_0^z \frac{(-\partial_r p(r, t))(h(r, t) - z') + \partial_r \sigma(r, t)}{\mu(r, z', t)} dz'. \quad (8)$$

Due to the non-constant viscosity, $u(r, z, t)$ depends non-locally on μ . The z -velocity w can be obtained by integrating (5) over z with $w|_{z=0} = 0$. Finally, employing the kinematic boundary condition at the interface, $\partial_t h + (\partial_r h)u|_{z=h} = w|_{z=h} + w_e$, the evolution of the droplet shape can be expressed as

$$\frac{\partial h}{\partial t} = \frac{1}{\rho|_{z=h}} \left[-\frac{1}{r} \frac{\partial}{\partial r} \int_0^h r \rho u dz - \int_0^h \frac{\partial \rho}{\partial t} dz \right] + w_e. \quad (9)$$

Here, $w_e(r, t)$ is the height change rate caused by evaporation, which is quantified in the following section.

2.4. Evaporation rate

For the derivation of the evaporation rate, the surrounding air is considered as additional component C. Furthermore, all quantities in the gas phase are denoted with a superscript g, whereas no superscript is used in the liquid. From the continuity equations for the individual species, the following jump conditions can be derived for $v = A, B, C$:

$$\dot{m}_v - \mathbf{J}_v \cdot \mathbf{n}_\Gamma - y_v \sum_{\xi=A,B,C} \dot{m}_\xi = 0 \quad (10)$$

$$\dot{m}_v - \mathbf{J}_v^g \cdot \mathbf{n}_\Gamma - y_v^g \sum_{\xi=A,B,C} \dot{m}_\xi = 0. \quad (11)$$

Here, $\dot{m}_v = y_v \rho (\mathbf{v}_v - \mathbf{v}_\Gamma) \cdot \mathbf{n}_\Gamma$ is the evaporative mass flux of component v , where \mathbf{v}_v is the velocity of species v , \mathbf{v}_Γ is the interface

velocity and \mathbf{n}_Γ the interface normal pointing to the gas phase. Eqs. (10) and (11) couple the evaporative mass fluxes \dot{m}_v with the diffusive fluxes \mathbf{J}_v and \mathbf{J}_v^g in both phases. Air is assumed to be only present in the gas phase, i.e. $y_C = 0$ and $\dot{m}_C = 0$. While in the binary liquid $\mathbf{J}_v = -\rho D_{AB} \nabla y_v$ holds for $v = A, B$, a general treatment of the diffusion in the ternary gas mixture is given by the Maxwell-Stefan relations. However, when the ambient temperature is far below the boiling point, the vapor concentrations y_A^g and y_B^g are much lower than y_C^g , i.e. $y_A^g, y_B^g \ll 1 \approx y_C^g$. This allows the usage of the Fickian limit $\mathbf{J}_v^g = -\rho^g D_{vC}^g \nabla y_v^g$ with the vapor diffusivity D_{vC}^g [32]. For the same reason, Eq. (11) decouples to the vapor diffusion-limited evaporation rates $\dot{m}_v = \mathbf{J}_v^g \cdot \mathbf{n}_\Gamma$ for $v = A, B$.

A time-scale analysis by Deegan et al. [5] and Hu and Larson [33] revealed that the vapor diffusion for single component droplets can be considered as instantaneous, which results, combined with the assumption of no air flow, in a Laplace equation for the vapor concentration. In Section 5.5.3, we substantiate that this assumption can also be applied to mixtures.

By assuming constant gas density ρ^g and using the ideal gas law $\rho_v^g = \rho^g y_v^g = p_v M_v / (R_u T)$, the evaporation rate is given by

$$\dot{m}_v = -\frac{D_{vC}^g M_v p_{\text{sat},v}}{R_u T} \frac{\partial \hat{p}_v}{\partial n_\Gamma}, \quad (12)$$

where $\hat{p}_v = \frac{p_v}{p_{\text{sat},v}}$ has to satisfy

$$\nabla^2 \hat{p}_v = 0, \quad (13)$$

with the molar mass M_v , the homogeneous saturation pressure $p_{\text{sat},v}$, the universal gas constant R_u and the temperature T . For a droplet consisting of a pure fluid v with a contact line radius r_c , the boundary conditions for (13) read

$$\hat{p}_v = 1 \quad \text{for } z = h(r, t) \text{ and } r < r_c \quad (14)$$

$$\partial_z \hat{p}_v = 0 \quad \text{for } z = 0 \text{ and } r > r_c \quad (15)$$

$$\hat{p}_v = RH_v \quad \text{for } (r, z) \rightarrow \infty. \quad (16)$$

Eqs. (14)–(16) represent saturated vapor at the liquid-air interface, no vapor penetration into the substrate and ambient relative humidity far away from the droplet, respectively. The evaporation rate \dot{m}_v is the same as used in Refs. [5,6,10].

In the case of a liquid mixture, the first boundary condition (14) has to be replaced by Raoult's law generalized to non-ideal mixtures, i.e.

$$\hat{p}_v = \gamma_v x_v \quad \text{for } z = h(r, t) \text{ and } r < r_c, \quad (17)$$

where $x_v(r, t)$ is the mole fraction of species v in the liquid and $\gamma(r, t) = \gamma_v(x_v(r, t))$ is the activity coefficient, which accounts for non-ideal interactions of the species.

Since x_v is in general non-homogeneous along the interface, the solution of (13) is more complicated than for a pure fluid. As depicted in Fig. S.5, a non-uniform composition at the interface can strongly enhance the evaporation of species v at positions with high $\gamma_v x_v$, whereas even for dry ambient air ($RH_v = 0$) condensation, i.e. $\dot{m}_v < 0$, may in principle happen at positions with low $\gamma_v x_v$.

The evaporation velocity w_e in (9) can finally be expressed as:

$$w_e = -\frac{\dot{m}_A + \dot{m}_B}{\rho|_{z=h}} \sqrt{1 + \left(\frac{\partial h}{\partial r} \right)^2}. \quad (18)$$

For a rigorous application of lubrication theory, the boundary condition (14) has to be evaluated at $z = 0$ instead of $z = h(r, t)$ and the square root in (18) is approximated by unity. An outline of the numerical implementation is given in Section S.1.

3. Results for water-glycerol droplets

While the model is most general, representative results are discussed on the basis of water-glycerol droplets in this section, whereas water-ethanol droplets are considered in the next section. We denote water as component A and glycerol as B. In order to model the composition-dependence of the physical properties, we have fitted experimental data for D_{AB} [34], σ and ρ [35] and used the model of Cheng [36] for the viscosity μ . The activity coefficients γ_i were calculated by the thermodynamic model AIOMFAC¹ [37,38]. The resulting functional relationships are depicted in Fig. S.1.

The temperature was set to $T = 25^\circ\text{C}$. Due to the very low vapor pressure of glycerol $p_{\text{sat},B} = 0.02\text{ Pa}$ [39], the evaporation of glycerol can be neglected on the considered timescales. For water, the vapor diffusion coefficient $D_{AC}^g = 0.26\text{ cm}^2/\text{s}$ [40] and the saturation pressure $p_{\text{sat},A} = 3.17\text{ kPa}$ [41] were used.

In Fig. 2, the spatio-temporal evolution of a 100 nL droplet with an initial contact angle of $\theta = 25^\circ$, a pinned contact line, dry air ($RH_A = 0$) and an initial composition of 75% water + 25% glycerol in terms of mass fractions is depicted. At the interface, water evaporates leading to an increased glycerol concentration. Due to the preferential evaporation near the contact line and the fact that the surface tension decreases with an increasing glycerol concentration, a Marangoni flow from the contact line to the top of the droplet is induced. We calculated the solutal Marangoni number Ma_s by

$$Ma_s = \frac{r_c}{\mu D_{AB}} (y_A|_{\text{apex}} - y_A|_{r_c}) \frac{\partial \sigma}{\partial y_A}, \quad (19)$$

where the viscosity and diffusivity were averaged over the volume. Typical solutal Marangoni numbers for water-glycerol droplets were found to be on the order of 10^4 .

When the droplet gets flat, the shape differs from the usual spherical cap due to the non-uniform surface tension. Therefore, although a pinned contact line is imposed, the liquid-air interface temporarily collapses with the substrate. When the surface tension gradient declines with the vanishing water content, the droplet relaxes again to the usual shape.

With decreasing water content evaporation slows down. Together with the vast viscosity increase of the remaining glycerol content, this results in a stagnation of the flow at later times. A small residual amount of water that can only reach the interface by diffusive transport is entrapped by a pure glycerol shell. Since the diffusion coefficient D_{AB} is reduced by a factor of approximately 50 in the limit of pure glycerol, the diffusive transport in the liquid is also slowed down.

The corresponding evolution of the droplet volume $V(t)$ is depicted for various relative humidities RH_A in Fig. 3(a). For completely dry air, i.e. $RH_A = 0$, the total volume V asymptotically approaches the glycerol volume $V_B^0 \approx 21\text{ nL}$. For higher relative humidities, the final volume increases because of the vapor-liquid equilibrium condition (17). For the same reason, the overall evaporation is drastically reduced for higher humidity RH_A , as can be inferred from the volume evolution of corresponding pure water droplets (dashed lines). At $RH_A \approx 93.5\%$, the droplet will not evaporate at all since the initial composition coincides with the vapor-liquid equilibrium.

To quantify the intensity of the Marangoni flow, the averaged tangential interface velocity is plotted in Fig. 3(b). This quantity is defined as

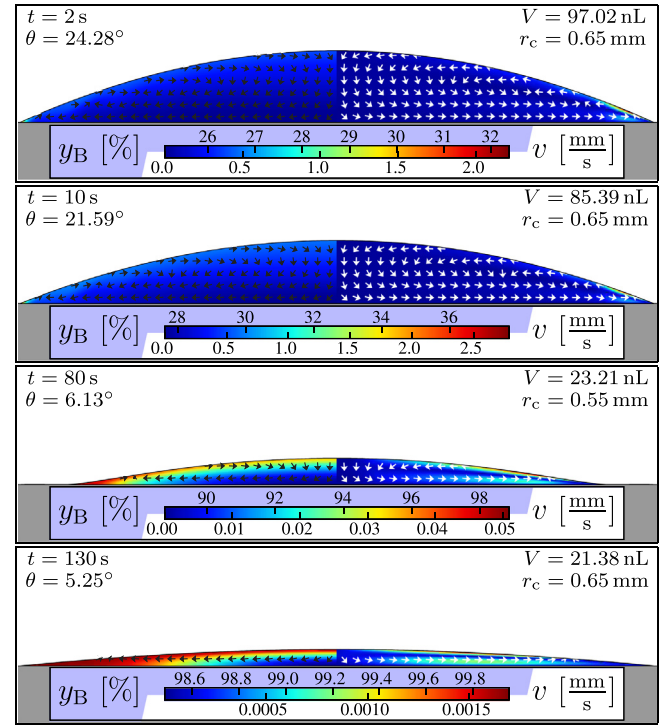


Fig. 2. Evaporation of a 100 nL droplet initially consisting of 75% water + 25% glycerol in terms of mass fractions in dry air. On each panel, the glycerol mass fraction y_B (left side) and the velocity (right side) are shown. The flow direction is indicated by the arrows.

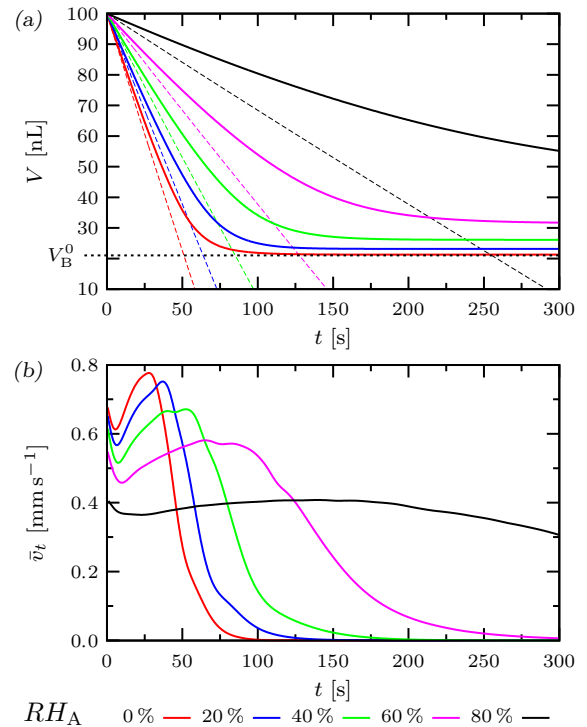


Fig. 3. Evolution of 100 nL droplets (75% water + 25% glycerol in terms of mass fractions) with a pinned contact line and $\theta(t=0) = 25^\circ$ at different relative humidities (solid lines). (a) Volume evolution, where the dashed lines indicate the evaporation of a pure water droplet at the same conditions. (b) Averaged tangential interface velocity v_t as quantification of the induced Marangoni flow.

¹ <http://www.aiomfac.caltech.edu>.

$$\bar{v}_t = \langle \mathbf{v} \cdot \mathbf{t}_\Gamma \rangle_\Gamma = \frac{\int_0^{r_c} \mathbf{t}_\Gamma \cdot \mathbf{v} |_{z=h(r,t)} \sqrt{1 + \left(\frac{\partial h}{\partial r}\right)^2} r dr}{\int_0^{r_c} \sqrt{1 + \left(\frac{\partial h}{\partial r}\right)^2} r dr} \quad (20)$$

with the interface average denoted by $\langle \dots \rangle_\Gamma$ and the tangential vector \mathbf{t}_Γ pointing from the contact angle towards the apex of the droplet (cf. Fig. 1). For dry air, \bar{v}_t is initially the highest, but the Marangoni flow ceases very quickly when almost only glycerol is remaining. This fast decay of \bar{v}_t can be attributed to the vast increase of the viscosity and the vanishing composition gradient along the liquid-air interface.

Droplet evolutions with an unpinned contact line are discussed in Section S.4.2.

4. Results for water-ethanol droplets

4.1. Numerical results

In the previous section, a water-glycerol mixture has been studied, where glycerol was assumed not to evaporate at all. In this section, a water-ethanol mixture where both components evaporate with different volatilities will be examined. We denote water by A and ethanol by B.

The composition-dependence of the physical properties were again modeled by fits of the corresponding data of Refs. [42–44]. The fits are depicted in Fig. S.2. Most notably, besides the strong compositional variation of the surface tension, is the activity coefficient of ethanol γ_B in the limit of pure water, i.e. $x_B \rightarrow 0$. Due to the enhanced activity of $\gamma_B \approx 5$, ethanol can evaporate rather quickly even at high dilution. The saturation pressure and vapor diffusion coefficient for ethanol read $p_{\text{sat},B} = 7.968 \text{ kPa}$ [45] and $D_{BC}^g = 0.135 \text{ cm}^2/\text{s}$ [40].

The evolution of a 100 nL droplet initially consisting of 50% water + 50% ethanol in terms of mass fractions with an initial contact angle $\theta = 25^\circ$ and a pinned contact line is depicted in Fig. 4. The relative humidities were set to $RH_A = 20\%$ and $RH_B = 0\%$. As in the case of water-glycerol droplets, the more volatile component, here ethanol, predominantly evaporates at the contact line. However, since ethanol has a lower surface tension than the less volatile water, the Marangoni flow with solutal Marangoni numbers on the order of -10^5 is now directed the other way round, i.e. from the top of the droplet along the liquid-air interface to the contact line. In a transient time at the beginning, a Marangoni-Bénard instability (cf. [46]) induces multiple vortices, but these merge with ongoing time.

In the long-time limit, when the ethanol has almost entirely evaporated, there is still a considerable Marangoni flow. However, in this regime, thermal Marangoni flow may also become relevant (cf. Section 4.2.2). When the droplet becomes flat, the surface tension gradient leads again to a shape deformation, but here with a depression at the droplet center. A similar phenomenon has been observed experimentally in flat alkane mixture droplets, where the central part actually dried before the remaining liquid ring [28].

In comparison to the water residual in the water-glycerol droplet, an appreciable entrapped ethanol residual at later times cannot be noticed, which can primarily be attributed to the strong convective mixing due to the fast Marangoni flow. Since the diffusion coefficient D_{AB} remains moderate in the water-ethanol droplet, the diffusive transport is also enhanced in comparison to the final stages of the water-glycerol droplet.

The volume evolution and mean tangential interface velocity \bar{v}_t for 100 nL water-ethanol droplets (50% water + 50% ethanol in terms of mass fractions) with a pinned contact line are depicted

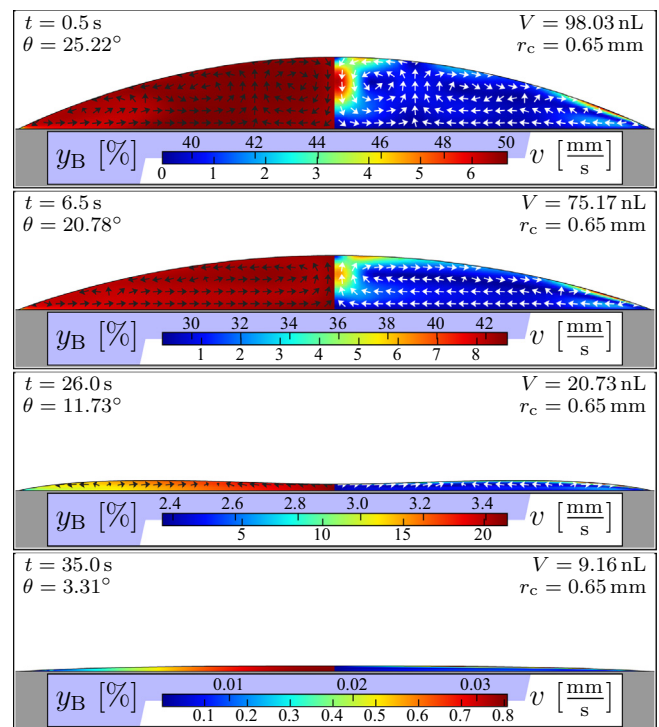


Fig. 4. Evaporation of a 100 nL droplet initially consisting of 50% water + 50% ethanol in terms of mass fractions with $RH_A = 20\%$ and $RH_B = 0\%$. On each panel, the ethanol mass fraction y_B (left side) and the velocity (right side) are shown. The flow direction is indicated by the arrows.

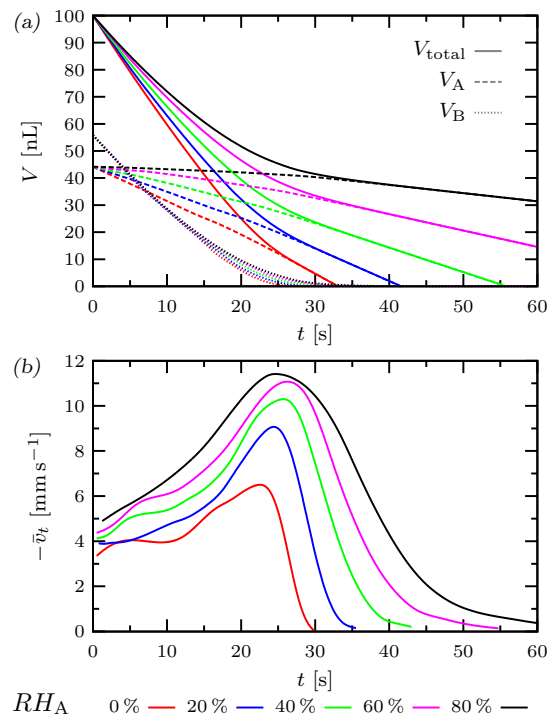


Fig. 5. Evolution of 100 nL water-ethanol droplets (50% water + 50% ethanol in terms of mass fractions) with a pinned contact line and $\theta(t=0) = 25^\circ$ at different relative humidities RH_A . (a) Volume evolution of the partial volumes V_v (water: dashed lines, ethanol: dotted lines) and the total volume V (solid lines). (b) Averaged tangential interface velocity \bar{v}_t as quantification of the induced Marangoni flow (here plotted as $-\bar{v}_t$ due to flow from the apex to the contact line).

in Fig. 5. While the total volume $V(t)$ is the actual volume of the droplet, the partial volumes $V_v(t)$ with $v = A, B$ are defined as

$$V_v = \frac{m_v / \rho_v^0}{m_A / \rho_A^0 + m_B / \rho_B^0} V, \quad (21)$$

where $m_v(t) = \int_{V(t)} y_v(\mathbf{r}, t) \rho(\mathbf{r}, t) dV$ is the total mass of component v in the droplet and ρ_v^0 is the mass density of the pure liquid v . With this definition $V = V_A + V_B$ holds, but due to the non-ideality, the droplet does in general not consist of a mixture of the volume V_A of pure water and the volume V_B of pure ethanol.

It is apparent from Fig. 5 that the evaporation can be separated into two stages: initially, the volume loss stems predominantly from the evaporation of the more volatile ethanol content. This contribution is basically independent of the relative humidity of water. After a rather sharp transition in the volume loss, the remaining pure water droplets evaporate at the expected rates. This sharp transition can be attributed to the highly non-ideal activity coefficients, since the same simulations with the ideal case of Raoult's law ($\gamma_A = \gamma_B = 1$) show a far smoother transition. For very high relative humidities, i.e. $RH_A > 84.2\%$ for this particular mixture, there is condensation of water in the initial stage as experimentally observed by Innocenzi et al. [20].

Initially, the induced Marangoni flow increases over time, which can be attributed to three facts: In the first place, the decreasing contact angle provides a more pronounced singularity near the contact line and thus a larger composition gradient. Secondly, the composition-dependence of the surface tension exhibits a steep slope with vanishing ethanol concentration (cf. Fig. S.2) so that the surface tension gradient is enhanced and, in the third place, the viscosity decreases in this limit.

With increasing water humidity RH_A , the mean Marangoni flow becomes in total faster. On the one hand, this is a result of the enhanced composition gradient. On the other hand, at a fixed time t , the volume $V(t)$ and thereby the height $h(r, t)$ will be larger for higher water humidities. As a consequence, the absolute influence of the shear stress boundary condition $\mu \partial_z u = \partial_r \sigma$ in (8) is enhanced. Although there is virtually no ethanol present at $t > 35$ s, a minimal amount of ethanol can still drive a considerable Marangoni flow.

A water-ethanol droplet with an unpinned contact line is discussed in Section S.4.3.

4.2. Comparison with experiments

4.2.1. Evaporation rate

There are several experimental studies on water-ethanol droplets in the literature. However, our model cannot be applied to the experiments where the contact angle θ reaches 90° or higher [16,17,19,22]. The experiments of Christy et al. [23] and Bennacer and Sefiane [24], however, have contact angles in the range of 6.6 – 25° . Unfortunately, the ambient conditions are not exactly specified in these articles. We have chosen reasonable values $T = 20^\circ\text{C}$, $RH_A = 40\%$ and $RH_B = 0\%$ for the ambient temperature and the relative humidities of water and ethanol, respectively. The saturation pressures $p_{\text{sat},v}$ were calculated at this temperature based on the Antoine equation taking the parameters from literature [45].

The volume losses $-\dot{V}(t)$ of two $0.12\ \mu\text{L}$ water-ethanol droplets with an initial ethanol content of 5% and 25% in terms of volume fraction and pinned base radii of $0.9\ \text{mm}$ and $1.0\ \text{mm}$, respectively, are depicted in Fig. 6 along with the corresponding data extracted from the experiments of Bennacer and Sefiane [24]. Since the time scale t_f used for the normalization is not explicitly specified in their article, we set it to $t_f = 115\ \text{s}$ based on the drying time of the droplet with 5% ethanol. It is apparent from Fig. 6 that our model can

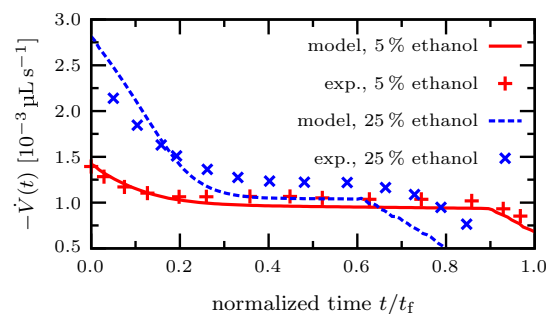


Fig. 6. Calculated volume losses $-\dot{V}(t)$ of $0.12\ \mu\text{L}$ water-ethanol droplets (lines) in comparison with the extracted experimental data (dots) of Ref. [24].

reproduce the initially enhanced evaporation rate due to the presence of ethanol. The following plateau is the evaporation rate of the droplet almost entirely consisting of water. In this regime, $-\dot{V}(t)$ is larger for the droplet with initially 25% ethanol. As already suspected in Ref. [24], this fact can be attributed to the different droplet geometries: Since the droplets with initially higher ethanol concentrations are flatter, the total evaporation rate is enhanced due to the larger surface area.

Towards the end of the lifetime of the droplet, the evaporation rate decreases, which can be presumably attributed to a receding of the contact line in the experiments. In our model, this receding is a necessary step in order to maintain numerical stability in the limit of very flat droplets. Due to the initial contact angle of $\theta \approx 6.6^\circ$, this numerical issue does not allow us to properly simulate the 50 – 50% droplet of Bennacer and Sefiane [24].

In total, however, the model is able to reproduce the experimental data for the volume loss. A better agreement could even be achievable if the exact ambient conditions of the experiments were known, the slightly moving contact line of the experiments would be considered and additional effects, e.g. the evaporative cooling, would be taken into account.

As shown in a recent study, a generalization of the model to ternary mixtures is able to reproduce the measured volume evolution and the onset of the oil emulsification (ouzo effect) of an ouzo droplet [47].

4.2.2. Concurrence of solutal and thermal Marangoni flow

In the following, the flow regimes in the droplet are compared with experimental findings. In the experiments of Christy et al. [23] and Bennacer and Sefiane [24], particle image velocimetry (PIV) was applied to measure the flow in a cross section parallel and close to the substrate. They observed an initially unordered flow with high vorticity in axial direction (regime I). After this, a short transition (regime II) with a decay of the vorticity and a sharp radial outward flow peak occurred, followed by the usual flow towards the pinned contact line (regime III).

Opposed to the short duration of regime II in those experiments, Zhong and Duan showed recently that regime II can actually last for a long part of the total drying time [25]. During this regime, they measured an inward radial flow close to the substrate, which can be attributed to an axisymmetric solutal Marangoni flow from the apex along the liquid-air interface towards the contact line.

Due to the assumption of axisymmetry, our model is not capable to reproduce the non-axisymmetric flow in regime I. Since the relative duration of the axisymmetric flows are longer in the experiments of Zhong and Duan, we focus on these in the following. Furthermore, the initial contact angles are moderate so that they are not affected by the afore-mentioned numerical stability issue for very flat droplets.

Until now, the evaporation process was assumed to be isothermal. For a detailed comparison with experiments, however, the latent heat of evaporation has to be considered to account for thermally driven Marangoni flow. For pure fluids, this issue has been raised by Sultan et al. [48] and was studied for pure sessile droplets by Dunn et al. [9,49]. In our model, the inclusion of thermal influences is achieved by considering the temperature equation

$$\rho c_p (\partial_t T + \mathbf{v} \cdot \nabla T) = \nabla \cdot (\lambda \nabla T) - (\Lambda_A \dot{m}_A + \Lambda_B \dot{m}_B) \delta_\Gamma, \quad (22)$$

where c_p is the specific heat capacity, λ the thermal conductivity and Λ_v the latent heat of evaporation. The quantities ρ , c_p and λ have different values in the three domains, i.e. droplet, air and substrate. The mass fraction weighted average of the corresponding values of the pure components were used for c_p and λ in the mixture. The appropriate values were taken from literature [45]. A possible influence of the Soret effect can be neglected due to the small Soret coefficient on the order of 10^{-3} [50].

Furthermore, the cooling at the liquid-air interface locally reduces the saturation pressure $p_{\text{sat},v}$. This can be expressed by the Antoine equation, but it has to be considered in the derivation of the evaporation rate in Section 2.4. As a result, the temperature field and the evaporation rate are coupled. The temperature-dependence of the physical properties were neglected, except for the surface tension. We have fitted the experimental data of Ref. [42] to obtain a functional relationship $\sigma(y_v, T)$.

The implementation of (22) into our model is a challenging task, since the thermal diffusivity is usually too large for explicit methods with feasible time steps. Therefore, we have implemented an *AutoMUG* multigrid method [51]. Unfortunately, this method suffers from numerical instabilities caused by the convective term, but the latter can be neglected, which can be argued as follows: In the initial regime, the flow is almost entirely constituted by solutal Marangoni flow so that a detailed consideration of the temperature will have only minor influences (cf. the following comparison of the Marangoni numbers). Once the ethanol content has almost entirely evaporated, thermal effects become the dominant driving force. In this regime, we have estimated the effect of the convective heat transport by finite element simulations of pure water droplets with and without convective term. It turned out that for these particular droplets the convective term can safely be neglected.

As in the experiments, we consider 0.2 μL -water-ethanol droplets with different initial compositions, a relative humidity of $RH_A = 50\%$ and an ambient temperature of $T = 23^\circ\text{C}$ [25]. To provide a direct comparison, the time t is normalized by the droplet lifetime t_{dry} as in the experiments, i.e. $\hat{t} = t/t_{\text{dry}}$.

Since the initial contact angle is rather high ($\approx 60^\circ$), the droplet is not well described by the parabolic equilibrium shape of the lubrication approximation. To that end, the square roots in (6) and (18) were not approximated by unity and the evaporation rate was calculated to the full order, i.e. not in the limit $h \rightarrow 0$. Despite being an inconsistent approximation, finite element simulations (cf. Section 5) revealed that the results with this generalized lubrication approximation are slightly more accurate for higher contact angles than the rigorous lubrication approximation.

In Fig. 7, we have depicted the evolution of a droplet with an initial amount of 20% ethanol in terms of volume fractions. Here, multiple vortices are initially present in regime I (Fig. 7(a)), but they merge to a single one later on (regime II). While the model cannot directly account for this transition due to the assumption of axisymmetry, we will focus on the following transition, regime II to III, in more detail.

As can be inferred from Fig. 7(b)–(d), thermal effects become relevant when almost all ethanol has evaporated. A new thermally driven vortex with reversed direction emerges near the contact

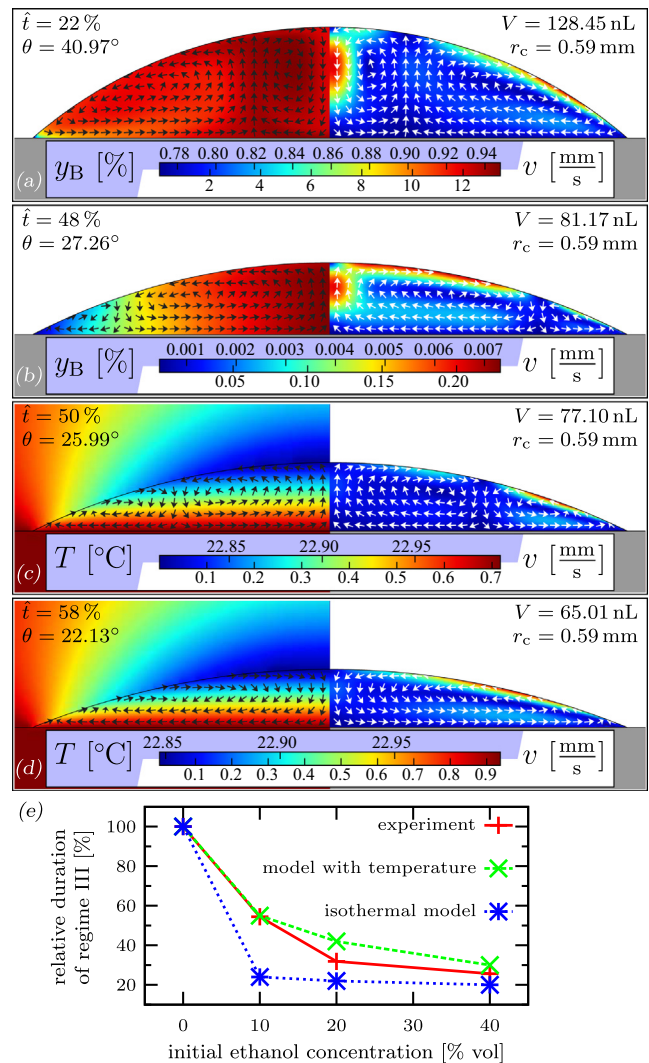


Fig. 7. Marangoni flow reversal in a water-ethanol droplet. (a) Initially, multiple vortices can be seen, which are driven by solutal Marangoni flow. With vanishing ethanol, thermal Marangoni flow becomes relevant and creates a new vortex near the contact line (b, c), which fills the entire droplet at the beginning of regime III (d). The left side of (a) and (b) show the ethanol concentration, while the temperature field is depicted in (c) and (d). (e) Relative duration of regime III for different initial ethanol concentrations experimentally measured by Zhong and Duan [25] and obtained by the model with and without consideration of thermal effects.

line and dominates the flow with ongoing time. Due to the high thermal conductivity of the silicon wafer substrate, the temperature gradient is not very pronounced and the substrate is virtually isothermal. The thermal Marangoni number Ma_{th} , defined by

$$Ma_{\text{th}} = \frac{r_c \rho c_p}{\mu \lambda} (T_{\text{apex}} - T_{\text{rc}}) \frac{\partial \sigma}{\partial T} \quad (23)$$

with the averaged thermal properties of the mixture, is on the order of 100 at the transition, whereas the solutal Marangoni number Ma_s is about -10^5 in the early stages of the evolution. The transition happens approximately when both numbers are comparable in magnitude.

The experimental data is confined to the flow close to the substrate. Therefore, outward radial flow in the entire droplet cannot be distinguished from a convection roll from the contact line along the liquid-air interface towards the apex in regime III. If a temperature field is considered in the model, we define the beginning of regime III as the time, when the thermally driven convection has

fully developed (cf. Fig. 7(d)). In the isothermal case, the beginning of regime III is defined at the moment when the typical outward radial flow throughout the entire droplet occurs.

The extracted data of the relative durations of regime III stemming from the experimental data of Zhong and Duan [25] is compared with the results of the model in Fig. 7(e): With increasing initial ethanol concentration, a solutally driven flow (regimes I and II) is present for a longer time during the drying, i.e. the duration of regime III is relatively shorter. This behavior is also reproduced by the model. However, in particular for small initial ethanol concentrations, the consideration of thermal effects is important for an accurate prediction of the duration of regime III. If the thermally driven Marangoni flow is not taken into account, a very dilute ethanol concentration can still drive a solutal Marangoni flow for a long time until the capillary outward radial flow becomes dominant towards the end of the drying time. We therefore conclude that the experimentally observed outward radial flow near the substrate in regime III is initially caused by thermal effects.

If thermal effects are considered in the model, the predicted duration of regime III is slightly longer than in the experiments. This difference can presumably be attributed to the fact that the transition time from regime II to III is very sensitive to the surface tension gradients in the limit of dilute ethanol, i.e. on $\partial\sigma/\partial y_B|_{y_B=0}$ and $\partial\sigma/\partial T|_{y_B=0}$. It is questionable whether the used fit of the experimental data is sufficiently accurate in this limit. Furthermore, the experimental error bars for the duration of regime III are not considered in Fig. 7(e), since they are not directly inferable from the data of Ref. [25].

Due to the high thermal conductivity of the substrate, the local cooling due to the latent heat has only a minor impact on the evaporation rates for the discussed droplets. The corresponding isothermal simulation of the evolution depicted in Fig. 7 predicts only 3.6% less time for the total drying.

5. Accuracy of the lubrication approximation

5.1. Comparison with a finite element method

As outlined in Section 2.3, our model takes advantage of a generalized lubrication approximation (LA) that simplifies the solution for the evolution of the flow field $\mathbf{v}(r, z, t)$ inside the droplet. In order to validate this approach and estimate the error stemming from this approximation, we have performed a comparison with a finite element method (FEM). For pure droplets, with and without temperature-driven Marangoni flow, this has already been done by Hu and Larson [7,8]. They concluded that the lubrication approach has an acceptable error for contact angles smaller than about $\theta = 40^\circ$.

Our comparison for binary mixture droplets was done as follows: At a distinct time t , we used the droplet shape $h(r)$ from the LA simulation to build a mesh with about 50,000 triangles. On this mesh, we solved the velocity field $\mathbf{v} = (u, w)$ without taking the lubrication limit but considering the corresponding Stokes flow. The latter reads in its strong form:

$$-\nabla \cdot \mathbf{T}(\mathbf{v}) = 0 \quad (24)$$

$$\nabla \cdot \mathbf{v} = 0 \quad (25)$$

with the stress tensor

$$\mathbf{T}(\mathbf{v}) = (-p\mathbf{I} + \mu(\nabla\mathbf{v} + (\nabla\mathbf{v})^t)). \quad (26)$$

For Eq. (25), we have assumed that the mass density is dominantly transported by advection, i.e. that $D\rho/Dt = 0$ holds, or, alternatively, that the mass density is slowly varying in space and time. In order to eliminate the error stemming from this assumption, we have

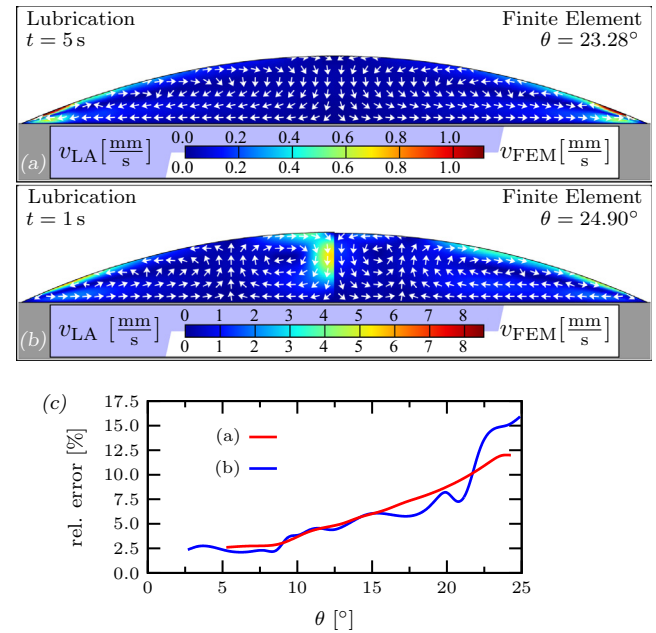


Fig. 8. Comparison of the flow calculated by the density-averaged lubrication approximation model (left side) and finite element method (right side). (a) Water-glycerol droplet from Fig. 2. (b) Same for the water-ethanol droplet evolution from Fig. 4. (c) The corresponding relative errors as function of the contact angle θ .

recalculated the LA simulations replacing the local mass density field $\rho(r, z, t)$ by an averaged value stemming from the spatial average of the mass fractions. The resulting droplet evolutions are virtually the same, so that a local consideration of the mass density is a detail of minor relevance. The temporal change of the average mass density is however important to reproduce a consistent volume evolution. The viscosity field $\mu(r, z)$ in (26) is taken from the LA simulation at the considered time. The flow is driven by the normal velocity v_n stemming from the kinematic relation

$$\mathbf{n}_\Gamma \cdot \mathbf{v} = \frac{\partial_t h - w_e}{\sqrt{1 + (\partial_r h)^2}} =: v_n \quad (27)$$

and the surface tension gradient $\partial_r \sigma(r)$. The corresponding data is also taken from the LA simulation. A detailed description of the FEM implementation can be found in Section 5.2.

In Fig. 8(a), (b), representative comparisons of the LA and the FEM calculations are shown on the basis of the droplet from Figs. 2 and 4, respectively. It can be seen that the LA calculations (left side) show qualitatively a similar flow field as the corresponding FEM simulations (right side). The LA results in a slightly higher velocity, which can primarily be attributed to the approximatively imposed shear stress (7). While the flow direction is in good agreement in the general case, a typical misprediction of the LA simulation is apparent from Fig. 8(b) near the droplet center $r = 0$, where the flow is much faster than in the FEM result. Since multiple vorticities are present due to a non-monotonic surface tension $\sigma(r)$, the characteristic lateral size is not the contact line radius r_c , but the width of a vortex. This leads to a higher aspect ratio by which the applicability of the lubrication approximation is limited. Since the flow is strongly coupled with the local composition, the initial chaotic flow phase of water-ethanol droplets (regime I) is probably inaccurately predicted by the LA simulation. When the flow has merged to a single vortex (regime II), the flow direction is qualitatively the same in both methods within the entire droplet.

In Fig. 8(c), the relative error of the velocity, defined by

$$\text{rel. error} = \frac{\|\mathbf{v}_{FEM} - \mathbf{v}_{LA}\|}{\|\mathbf{v}_{FEM}\|} \quad (28)$$

with

$$\langle \dots \rangle = \sqrt{\int_0^{r_c} r dr \int_0^{h(r)} dz (\dots)^2}, \quad (29)$$

is plotted for the corresponding simulations as a function of the contact angle θ . It can clearly be seen that the relative error for the water-glycerol droplet is about 12% at the initial contact angle $\theta = 25^\circ$. In comparison, for the thermally driven Marangoni flow of a 100 nL pure water droplet on a silicon substrate, an error of 12% can be found at a contact angle of $\theta \approx 40^\circ$. The higher error of the solutal Marangoni flow stems from the pronounced surface tension gradient $\partial_r \sigma$ near the contact line, which is less intense for thermal Marangoni flow. The water-ethanol droplet initially shows a higher error due to the presence of multiple vorticities.

6. Influence of Marangoni flow on the evaporation

Since the velocity field is coupled via the fluid composition with the evaporation rates and thus with the volume evolution, the latter is affected by the Marangoni flow. To investigate the influence of the convective solutal transport on the volume evolution, two extreme cases are considered: On the one hand, the solutal Marangoni flow can be artificially disregarded by replacing the local surface tension $\sigma(r, t)$ by its spatial average. This case represents the lower bound for the convective transport of the composition due to the absence of Marangoni flow, i.e. $Ma_s = 0$.

On the other hand, one can consider the case of a perfectly mixed droplet, which represents the case of an infinitely fast Marangoni flow ($Ma_s \rightarrow \infty$). In this limit, $y_v(r, z, t) = y_v(t)$ holds, which allows to generalize the model of Popov [6] from a pure droplet to mixture droplets as follows: The total mass of the droplet is constituted by the partial masses, i.e. $m(t) = m_A(t) + m_B(t)$. If the droplet is perfectly mixed and in a spherical cap shape, the derivation of Popov can be applied to the partial masses $m_v(t)$. The only difference is that Raoult's law (17) instead of saturated vapor has to be imposed at the liquid-air interface, i.e.

$$\frac{dm_v}{dt} = -\pi r_c f(\theta) \frac{D_{vc}^g M_v p_{\text{sat},v}}{R_u T} (\gamma_v x_v - RH_v) \quad (30)$$

with the geometric factor

$$f(\theta) = \frac{\sin \theta}{1 + \cos \theta} + 4 \int_0^\infty \frac{1 + \cosh(2\theta\tau)}{\sinh(2\theta\tau)} \tanh((\pi - \theta)\tau) d\tau. \quad (31)$$

Eq. (30) can be easily integrated numerically for $v = A, B$. At each time step, the mole fractions x_v have to be calculated from the mass fractions $y_v = m_v/m$ and the contact line r_c and contact angle θ are dependent on the volume $V = m/\rho$ and whether a pinned or an unpinned contact line is considered.

Fig. 9(a) shows the volume evolution $V(t)$ of water-glycerol droplets according to full simulations, simulations without Marangoni flow and according to the perfectly mixed model (30). Without Marangoni flow, the volatile water can reach the interface only by diffusion so that the evaporation is slower than in the full simulations with a maximum deviation of 5.3% with respect to $V_0 = 100$ nL. Conversely, the perfectly mixed model (30) cannot account for the entrapped water at later times (cf. Section 3), so that the evaporation in this model is faster. Here, the maximum deviation is 6.7%. Fig. 9(b) shows the curves for water-ethanol droplets. Due to the fast Marangoni flow in the full simulations, the perfectly mixed model reproduces the volume evolution almost exactly ($< 1.7\%$ deviation). This is remarkable, since the perfectly mixed model cannot account for the droplet deformation due to the assumption of a spherical cap shape. The maximum deviation of the simulations without Marangoni flow is 9.7%.

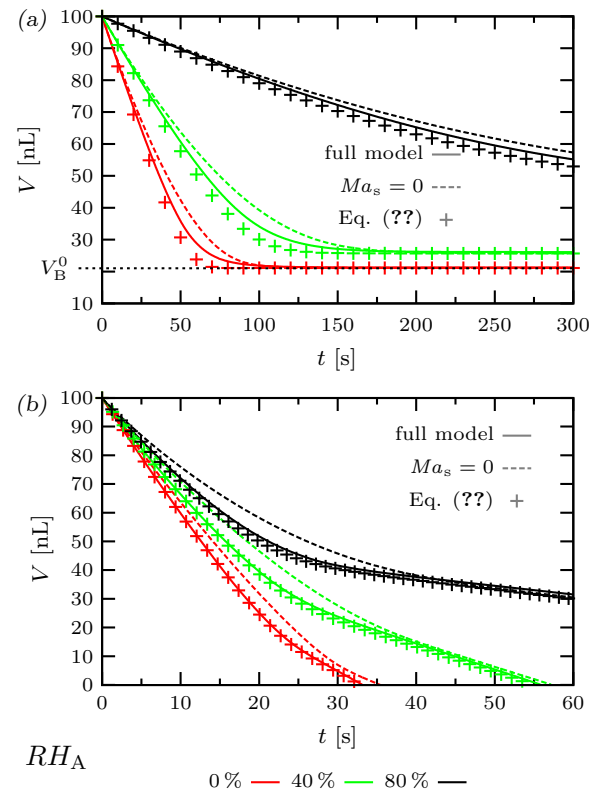


Fig. 9. Influence of Marangoni flow on the evaporation rate by comparing the full simulations (solid lines), simulations without Marangoni flow (dashed lines) and perfectly mixed droplets (+). (a) Water-glycerol droplets from Fig. 3. (b) Water-ethanol droplets from Fig. 5.

We conclude that the total evaporation rate is enhanced by Marangoni flow. In case of high Marangoni numbers Ma_s , e.g. water-ethanol droplets, the generalization of Popov's model provides an accurate method to determine the volume evolution $V(t)$ by solving the rather simple system of ODEs (30).

7. Conclusion

For the first time we have developed a numerical model for the drying of sessile binary mixture droplets, which has been investigated in numerous experimental studies [15–28]. The presence of two fluid components necessitates a generalization of the well-established vapor-diffusion limited evaporation model [4–6] by the incorporation of Raoult's law extended by activity coefficients at the liquid-air interface. Furthermore, the preferential evaporation of the more volatile component induces a non-homogeneous liquid composition, which couples via the composition-dependence of the physical properties of the mixture to a rather complicated spatio-temporal evolution.

We examined the evaporation of both water-glycerol and water-ethanol droplets. In both cases the enhanced evaporation of the more volatile component near the contact line induces a surface tension gradient, which drives a Marangoni flow and can lead to a deviation from the spherical cap shape for flat droplets. As a consequence of the Marangoni flow, the more volatile component is replenished at the liquid-air interface. In the case of water-glycerol droplets, however, the flow ceases due to the vast viscosity increase in the limit of pure glycerol. Because of the low mutual diffusion coefficient, the entrapped remaining amount of water is hampered to reach the interface and subsequently evaporate. In contrast, the surface tension gradient in the case of

water-ethanol droplets is more pronounced and the viscosity remains rather small. The Marangoni flow, here directed the other way round, is maintained until the ethanol content has almost completely evaporated. In this limit, thermal Marangoni flow can set in which results in a flow direction reversal. The model shows good agreement with experimental data of Bennacer and Sefiane [24] and Zhong and Duan [25]. Moreover, a generalization of the model is capable to reproduce the evaporation of a ternary ouzo droplet [47].

In a next step, the model will be generalized to take the deposition of colloidal particles and the presence of surfactants into account. That way, it can serve as a predictive tool for the production of homogeneous deposition patterns by controlling the Marangoni flow [25,26,52], which is of utmost relevance in inkjet printing applications.

Acknowledgments

This research is supported by the Dutch Technology Foundation STW, which is part of the Netherlands Organization for Scientific Research (NWO) and partly funded by the Ministry of Economic Affairs, Agriculture and Innovation. The authors gratefully acknowledge additional funding by Océ – A Canon Company. This work has been done under the umbrella of COST Action MP1106. The authors would like to thank Xin Zhong and Fei Duan for providing us with additional details about their experiments.

Appendix A. Supplementary material

Supplementary data associated with this article can be found, in the online version, at <http://dx.doi.org/10.1016/j.jcis.2016.10.030>.

References

- [1] M. Singh, H.M. Haverinen, P. Dhagat, G.E. Jabbour, Inkjet printing-process and its applications, *Adv. Mater.* 22 (6) (2010) 673–685, <http://dx.doi.org/10.1002/adma.200901141>.
- [2] J. Kim, Spray cooling heat transfer: the state of the art, *Int. J. Heat Fluid Flow* 28 (4) (2007) 753–767, <http://dx.doi.org/10.1016/j.ijheatfluidflow.2006.09.003>.
- [3] V. Dugas, J. Broutin, E. Souteyrand, Droplet evaporation study applied to DNA chip manufacturing, *Langmuir* 21 (20) (2005) 9130–9136, <http://dx.doi.org/10.1021/la050764y>.
- [4] R.D. Deegan, O. Bakajin, T.F. Dupont, G. Huber, S.R. Nagel, T.A. Witten, Capillary flow as the cause of ring stains from dried liquid drops, *Nature* 389 (6653) (1997) 827–829, <http://dx.doi.org/10.1038/39827>.
- [5] R. Deegan, O. Bakajin, T. Dupont, G. Huber, S. Nagel, T. Witten, Contact line deposits in an evaporating drop, *Phys. Rev. E* 62 (1) (2000) 756–765, <http://dx.doi.org/10.1103/physreve.62.756>.
- [6] Y. Popov, Evaporative deposition patterns: spatial dimensions of the deposit, *Phys. Rev. E* 71 (3) (2005), <http://dx.doi.org/10.1103/physreve.71.036313>.
- [7] H. Hu, R.G. Larson, Analysis of the microfluid flow in an evaporating sessile droplet, *Langmuir* 21 (9) (2005) 3963–3971, <http://dx.doi.org/10.1021/la047528s>.
- [8] H. Hu, R.G. Larson, Analysis of the effects of Marangoni stresses on the microflow in an evaporating sessile droplet, *Langmuir* 21 (9) (2005) 3972–3980, <http://dx.doi.org/10.1021/la0475270>.
- [9] G.J. Dunn, S.K. Wilson, B.R. Duffy, S. David, K. Sefiane, The strong influence of substrate conductivity on droplet evaporation, *J. Fluid Mech.* 623 (2009) 329, <http://dx.doi.org/10.1017/s0022112008005004>.
- [10] D.P. Siregar, J.G.M. Kuerten, C.W.M. van der Geld, Numerical simulation of the drying of inkjet-printed droplets, *J. Colloid Interface Sci.* 392 (2013) 388–395, <http://dx.doi.org/10.1016/j.jcis.2012.09.063>.
- [11] M.R. Barmi, C.D. Meinhardt, Convective flows in evaporating sessile droplets, *J. Phys. Chem. B* 118 (9) (2014) 2414–2421, <http://dx.doi.org/10.1021/jp408241f>.
- [12] J.M. Stauber, S.K. Wilson, B.R. Duffy, K. Sefiane, On the lifetimes of evaporating droplets, *J. Fluid Mech.* 744 (2014), <http://dx.doi.org/10.1017/jfm.2014.94>.
- [13] J.M. Stauber, S.K. Wilson, B.R. Duffy, K. Sefiane, Evaporation of droplets on strongly hydrophobic substrates, *Langmuir* 31 (12) (2015) 3653–3660, <http://dx.doi.org/10.1021/acs.langmuir.5b00286>.
- [14] P. Sáenz, K. Sefiane, J. Kim, O. Matar, P. Valluri, Evaporation of sessile drops: a three-dimensional approach, *J. Fluid Mech.* 772 (2015) 705–739, <http://dx.doi.org/10.1017/jfm.2015.224>.
- [15] S.M. Rowan, M.I. Newton, F.W. Driewer, G. McHale, Evaporation of microdroplets of azeotropic liquids, *J. Phys. Chem. B* 104 (34) (2000) 8217–8220, <http://dx.doi.org/10.1021/jp000938e>.
- [16] K. Sefiane, L. Tadrist, M. Douglas, Experimental study of evaporating water-ethanol mixture sessile drop: influence of concentration, *Int. J. Heat Mass Transfer* 46 (23) (2003) 4527–4534, [http://dx.doi.org/10.1016/s0017-9310\(03\)00267-9](http://dx.doi.org/10.1016/s0017-9310(03)00267-9).
- [17] A.K.H. Cheng, D.M. Soolaman, H.-Z. Yu, Evaporation of microdroplets of ethanol-water mixtures on gold surfaces modified with self-assembled monolayers, *J. Phys. Chem. B* 110 (23) (2006) 11267–11271, <http://dx.doi.org/10.1021/jp0572885>.
- [18] Z. Wang, X.-F. Peng, A.S. Mujumdar, A. Su, D.-J. Lee, Evaporation of ethanol-water mixture drop on horizontal substrate, *Dry. Technol.* 26 (6) (2008) 806–810, <http://dx.doi.org/10.1080/07373930802046526>.
- [19] L. Shi, P. Shen, D. Zhang, Q. Lin, Q. Jiang, Wetting and evaporation behaviors of water-ethanol sessile drops on PTFE surfaces, *Surf. Interface Anal.* 41 (12–13) (2009) 951–955, <http://dx.doi.org/10.1002/sia.3123>.
- [20] P. Innocenzi, L. Malfatti, S. Costacurta, T. Kidchob, M. Piccinini, A. Marcelli, Evaporation of ethanol and ethanol-water mixtures studied by time-resolved infrared spectroscopy, *J. Phys. Chem. A* 112 (29) (2008) 6512–6516, <http://dx.doi.org/10.1021/jp7111395>.
- [21] K. Sefiane, S. David, M.E.R. Shanahan, Wetting and evaporation of binary mixture drops, *J. Phys. Chem. B* 112 (36) (2008) 11317–11323, <http://dx.doi.org/10.1021/jp8030418>.
- [22] C. Liu, E. Bonaccorso, H.-J. Butt, Evaporation of sessile water/ethanol drops in a controlled environment, *Phys. Chem. Chem. Phys.* 10 (47) (2008) 7150, <http://dx.doi.org/10.1039/b808258h>.
- [23] J.R.E. Christy, Y. Hamamoto, K. Sefiane, Flow transition within an evaporating binary mixture sessile drop, *Phys. Rev. Lett.* 106 (20) (2011), <http://dx.doi.org/10.1103/physrevlett.106.205701>.
- [24] R. Bennacer, K. Sefiane, Vortices, dissipation and flow transition in volatile binary drops, *J. Fluid Mech.* 749 (2014) 649–665, <http://dx.doi.org/10.1017/jfm.2014.220>.
- [25] X. Zhong, F. Duan, Flow regime and deposition pattern of evaporating binary mixture droplet suspended with particles, *Eur. Phys. J. E* 39 (2) (2016), <http://dx.doi.org/10.1140/epje/i2016-16018-5>.
- [26] H. Kim, F. Boulogne, E. Um, I. Jacobi, E. Button, H.A. Stone, Controlled uniform coating from the interplay of Marangoni flows and surface-adsorbed macromolecules, *Phys. Rev. Lett.* 116 (12) (2016), <http://dx.doi.org/10.1103/physrevlett.116.124501>.
- [27] N.J. Ciria, A. Benusioglio, M. Prakash, Vapour-mediated sensing and motility in two-component droplets, *Nature* 519 (7544) (2015) 446–450, <http://dx.doi.org/10.1038/nature14272>.
- [28] G. Guéna, C. Poulard, A.M. Cazabat, Evaporating drops of alkane mixtures, *Colloid. Surface A* 298 (1–2) (2007) 2–11, <http://dx.doi.org/10.1016/j.colsurfa.2006.12.008>.
- [29] R. Bird, W.E. Stewart, E.N. Lightfoot, *Transport Phenomena*, J. Wiley, New York, 2007.
- [30] G.K. Batchelor, *An Introduction to Fluid Dynamics*, Cambridge University Press, Cambridge New York, 1973.
- [31] A. Oron, S.G. Bankoff, Long-scale evolution of thin liquid films, *Rev. Mod. Phys.* 69 (3) (1997) 931–980, <http://dx.doi.org/10.1103/revmodphys.69.931>.
- [32] R. Krishna, J.A. Wesselingh, The Maxwell-Stefan approach to mass transfer, *Chem. Eng. Sci.* 52 (6) (1997) 861–911, [http://dx.doi.org/10.1016/s0009-2509\(96\)00458-7](http://dx.doi.org/10.1016/s0009-2509(96)00458-7).
- [33] H. Hu, R.G. Larson, Evaporation of a sessile droplet on a substrate, *J. Phys. Chem. B* 106 (6) (2002) 1334–1344, <http://dx.doi.org/10.1021/jp0118322>.
- [34] G. D'Errico, O. Ortona, F. Capuano, V. Vitagliano, Diffusion coefficients for the binary system glycerol + water at 25 °C. A velocity correlation study, *J. Chem. Eng. Data* 49 (6) (2004) 1665–1670, <http://dx.doi.org/10.1021/je049917u>.
- [35] K. Takamura, H. Fischer, N.R. Morrow, Physical properties of aqueous glycerol solutions, *J. Petrol. Sci. Eng.* 98–99 (2012) 50–60, <http://dx.doi.org/10.1016/j.petrol.2012.09.003>.
- [36] N.-S. Cheng, Formula for the viscosity of a glycerol–water mixture, *Ind. Eng. Chem. Res.* 47 (9) (2008) 3285–3288, <http://dx.doi.org/10.1021/ie071349z>.
- [37] A. Zuend, C. Marcolli, B.P. Luo, T. Peter, A thermodynamic model of mixed organic-inorganic aerosols to predict activity coefficients, *Atmos. Chem. Phys.* 8 (16) (2008) 4559–4593, <http://dx.doi.org/10.5194/acp-8-4559-2008>.
- [38] A. Zuend, C. Marcolli, A.M. Booth, D.M. Lienhard, V. Soonsin, U.K. Krieger, D.O. Topping, G. McFiggans, T. Peter, J.H. Seinfeld, New and extended parameterization of the thermodynamic model AIOMFAC: calculation of activity coefficients for organic-inorganic mixtures containing carboxyl, hydroxyl, carbonyl, ether, ester, alkenyl, alkyl, and aromatic functional groups, *Atmos. Chem. Phys.* 11 (17) (2011) 9155–9206, <http://dx.doi.org/10.5194/acp-11-9155-2011>.
- [39] H.K. Cammenga, F.W. Schulze, W. Theuerl, Vapor pressure and evaporation coefficient of glycerol, *J. Chem. Eng. Data* 22 (2) (1977) 131–134, <http://dx.doi.org/10.1021/je60073a004>.
- [40] C.Y. Lee, C.R. Wilke, Measurements of vapor diffusion coefficient, *Ind. Eng. Chem.* 46 (11) (1954) 2381–2387, <http://dx.doi.org/10.1021/ie50539a046>.
- [41] W.M. Haynes, *CRC Handbook of Chemistry and Physics*, CRC Press, 2014.
- [42] G. Vazquez, E. Alvarez, J.M. Navaza, Surface tension of alcohol water + water from 20 to 50 °C, *J. Chem. Eng. Data* 40 (3) (1995) 611–614, <http://dx.doi.org/10.1021/je00019a016>.
- [43] B. González, N. Calvar, E. Gómez, A. Domínguez, Density, dynamic viscosity, and derived properties of binary mixtures of methanol or ethanol with water, ethyl acetate, and methyl acetate at T = (293.15, 298.15, and 303.15) K, *J. Chem. Thermodyn.* 39 (12) (2007) 1578–1588, <http://dx.doi.org/10.1016/j.jct.2007.05.004>.

- [44] S. Pañez, G. Guevara-Carrion, H. Hasse, J. Vrabec, Mutual diffusion in the ternary mixture of water + methanol + ethanol and its binary subsystems, *Phys. Chem. Chem. Phys.* 15 (11) (2013) 3985, <http://dx.doi.org/10.1039/c3cp43785j>.
- [45] J. Dean, *Lange's Handbook of Chemistry*, McGraw-Hill, New York, 1992.
- [46] H. Machrafi, A. Rednikov, P. Colinet, P. Dauby, Bénard instabilities in a binary-liquid layer evaporating into an inert gas, *J. Colloid Interface Sci.* 349 (1) (2010) 331–353, <http://dx.doi.org/10.1016/j.jcis.2010.04.043>.
- [47] H. Tan, C. Diddens, P. Lv, J.G.M. Kuerten, X. Zhang, D. Lohse, Evaporation-triggered microdroplet nucleation and the four life phases of an evaporating Ouzo drop, *Proc. Natl. Acad. Sci. USA* 113 (31) (2016) 8642, <http://dx.doi.org/10.1073/pnas.1602260113>.
- [48] E. Sultan, A. Boudaoud, M. ben Amar, Evaporation of a thin film: diffusion of the vapour and Marangoni instabilities, *J. Fluid Mech.* 543 (2005) 183, <http://dx.doi.org/10.1017/s0022112005006348>.
- [49] G.J. Dunn, S.K. Wilson, B.R. Duffy, K. Sefiane, Evaporation of a thin droplet on a thin substrate with a high thermal resistance, *Phys. Fluids* 21 (5) (2009) 052101, <http://dx.doi.org/10.1063/1.3121214>.
- [50] J.K. Platten, M.M. Bou-Ali, P. Blanco, J.A. Madariaga, C. Santamaria, Soret coefficients in some water-methanol, water-ethanol, and water-isopropanol systems, *J. Phys. Chem. B* 111 (39) (2007) 11524–11530, <http://dx.doi.org/10.1021/jp074206z>.
- [51] Y. Shapira, *Matrix-based Multigrid Theory and Applications*, Springer, New York, NY, 2008.
- [52] M. Majumder, C.S. Rendall, J.A. Eukel, J.Y.L. Wang, N. Behabtu, C.L. Pint, T.-Y. Liu, A.W. Orbaek, F. Mirri, J. Nam, Overcoming the coffee-stain effect by compositional Marangoni-flow-assisted drop-drying, *J. Phys. Chem. B* 116 (22) (2012) 6536–6542, <http://dx.doi.org/10.1021/jp3009628>.